Journal of Quantitative Spectroscopy & Radiative Transfer 350 (2026) 109761

Contents lists available at ScienceDirect

Journal of Quantitative Spectroscopy and Radiative Transfer

journal homepage: www.elsevier.com/locate/jqsrt

Study of linear depolarization ratios across a wide range of scattering angles for particles of diverse sizes, shapes, and complex refractive indices

Prakash Gautam [a,*], Justin B. Maughan [b], Hans Moosmüller [a], Kurt Ehlers [c], Christopher M. Sorensen [d]

[a] Laboratory for Aerosol Science, Spectroscopy, and Optics, Desert Research Institute, Nevada, System of Higher Education, 2215 Raggio Parkway, Reno, NV 89512, USA
[b] Pratt Community College, 348 NE SR 61, Pratt, KS 67124, USA
[c] Mathematics Department, Truckee Meadows Community College, 7000 Dandini Blvd., Reno, NV 89512, USA
[d] Department of Physics, Kansas State University, 116 Cardwell Hall, 1228 N. 17th Street, Manhattan, KS 66506, USA

ARTICLE INFO

Keywords:
Polarimetry
Particle scattering
Complex refractive index
Wide-angle
Linear Depolarization Ratio
Remote Sensing

ABSTRACT

Polarimetry is a valuable technique for remote sensing of atmospheric aerosol particles, with the linear depolarization ratio (LDR) being a key parameter used to characterize particle properties. This study investigates the LDRs of various aerosol particles, including nearly spherical and irregular aluminum oxide (Al_2O_3), Arizona Road Dust (AZRD), and molybdenum disulfide (MoS_2) particles, using both laboratory measurements conducted at a wavelength of 532 nm over a scattering angle range from 0.32° to 177.6° and theoretical model computations for spheroids and Gaussian random spheres. The results demonstrate that the LDR is strongly influenced by particle size, shape, and refractive index, with significant variations across different scattering angles. In the forward-scattering regime, LDR values are small due to scattering being dominated by diffraction, while in the side-scattering regime, LDR increases, peaking around 140° to 160°, before decreasing in the back-scattering regime. This study further explores the relationship between LDR and particle morphology, as well as the impact of the imaginary part of the complex refractive index on LDR, with results showing that higher absorption leads to lower LDRs. Overall, this study contributes to a better understanding of how LDR behaves for different particle types and scattering angles, enhancing our understanding of the optical properties of aerosol particles towards improved polarimetric remote sensing retrievals.

1. Introduction

Polarimetry is an important remote sensing technique for characterizing atmospheric aerosol particles [1]. The linear depolarization ratio (LDR) is a parameter in polarimetry that characterizes how much the polarization state of light changes as it interacts with scattering particles. The single scattering LDR depends on particle morphology, including shape, size, and complex refractive index (CRI), and on the scattering angle; it is a fundamental measure of a particle's non-sphericity and homogeneity. Non-spherical particles generally have non-zero LDRs due to differential scattering that arises predominantly from the internal light reflection within the particles. Analyzing LDR can provide valuable information about physical and optical properties of scattering particles and, hence, be useful for remote sensing retrievals including the classification of aerosol particle types 2,3.

This paper focuses on laboratory measurements of LDRs for various aerosol particles, including nearly spherical and irregular aluminum oxide (Al_2O_3), irregular Arizona Road Dust (AZRD), and highly refractive, plate-like molybdenum disulfide (MoS_2) particles, along with theoretical calculations to interpret the measured data. We selected these particles because they are well-characterized, readily accessible, and scientifically representative of a broad range of atmospheric aerosols. Specifically, the refractive indices of Al_2O_3 and (AZRD) closely approximate those of naturally occurring mineral dust particles found in the atmosphere, making them ideal for comparative optical studies. Additionally, molybdenum disulfide (MoS_2) is both highly refractive and strongly absorptive, providing an upper boundary condition for the complex refractive index spectra of aerosol particles. By incorporating such diverse materials, ranging from weakly to strongly absorbing and refracting, we aim to broaden our intellectual framework and develop a

* Corresponding author.
E-mail addresses: Prakash.Gautam@dri.edu (P. Gautam), justinm@prattcc.edu (J.B. Maughan), Hans.Moosmuller@dri.edu (H. Moosmüller), kehlers@tmcc.edu (K. Ehlers), sor@phys.ksu.edu (C.M. Sorensen).

https://doi.org/10.1016/j.jqsrt.2025.109761
Received 25 March 2025; Received in revised form 20 November 2025; Accepted 20 November 2025
Available online 21 November 2025

more comprehensive understanding of how optical properties vary across different particle systems. This approach enhances our ability to interpret angular scattering behavior and improve aerosol modeling for environmental and atmospheric applications.

Investigations of light scattering and linear depolarization ratio (LDR) measurements by irregularly shaped aerosol particles are “neither few nor small”, e.g. 4–12. However, most of these efforts have focused on specific aspects of the scattering process, often limited to non-absorbing particles or constrained to narrow angular ranges, such as exact or near-backscattering directions (i.e., close to 180°). While valuable, these approaches do not fully capture the angular scattering behavior of complex particles. In contrast, our study offers a more comprehensive perspective by performing simultaneous light scattering measurements over a near-complete angular range, capturing data from ~0.32° to ~177.6° This wide-angle, high-resolution approach enables a more detailed analysis of how particle shape, size, and composition influence scattering and depolarization, addressing key gaps in aerosol optics and remote sensing models. Measurements were performed at a visible wavelength of 532 nm. The experimental data were analyzed using theoretical simulations, where particle optics was modeled using Gaussian random sphere, spheroid, and other shapes with T-matrix calculations [13]. Our experimental and theoretical results consistently demonstrate significantly low LDR values in the forward-scattering regime, where diffraction plays a dominant role. Subsequently, the LDR values progressively increased with scattering angle, reaching a peak at around 140° to 160° in the side-scattering regime before declining in the back-scattering regime. Overall, our results indicate that LDR strongly depends on particle size, shape, and refractive index along with scattering angle.

2. Materials and methods

The particles investigated here include nearly spherical-to-irregular aluminum abrasive (Al_2O_3), spherical silica (SiO_2), Arizona road dust (AZRD), and highly refractive molybdenum disulfide (MoS_2) particles. We additionally analyzed some of the angular scattering data available in the Granada-Amsterdam (G/A) light scattering database [10,14]. We investigated the particles’ shape using optical and transmission electron microscopy, as shown in Fig. 1. The shape of particles with sizes not shown in Fig. 1 and their size distribution can be found in [5] for AZRD and in [15] for Al_2O_3. The microscope images indicate that SiO_2 particles are fairly spherical, with nano-sized spherical particles attached to near-spherical micron-size particles, whereas the MoS_2, AZRD, and Al_2O_3 particles are much more irregularly shaped.

Fig. 2 gives the schematic of the experimental light scattering setup. A detailed description of the experimental setup and data procurement methods can be found in [17]. In short, the whole angularly resolved light scattering setup can be divided into three regimes: forward-, side-, and back-scattering. The forward-scattering setup is based on a design by Ferri (1997) [18], which consists of a Fourier lens, beam stop, and imaging lens as the main components and collects the scattered light from 0.32° to 9.89°. The side-scattering part of the setup includes an elliptical mirror, iris, and collimating lens and collects the scattered light from 15° to 157°, whereas the back-scattering setup consists of a 90° off-axis parabolic mirror with a 3-mm hole parallel to the incident beam, that collects the back-scattered light from 158° to 177.6°. The two 16-channel photomultiplier tube (PMT) detector arrays simultaneously collect scattered light at 31 angles, for a total of 47 angles from 0.32° to 177.6° Additionally, this experimental design includes an aerodynamic particle sizer (APS) providing a real-time measurement of the most probable size of the aerosols and their size distribution spread in the scattering volume. This allowed us to compare theoretical calculations with in-situ laboratory measurements. Each and inter-detector calibration was performed with light scattered from gases with known Rayleigh ratios [19].

The light used for the experiment is vertically polarized at a wavelength of 532 nm, and the LDR for this incident light is given by [20] as

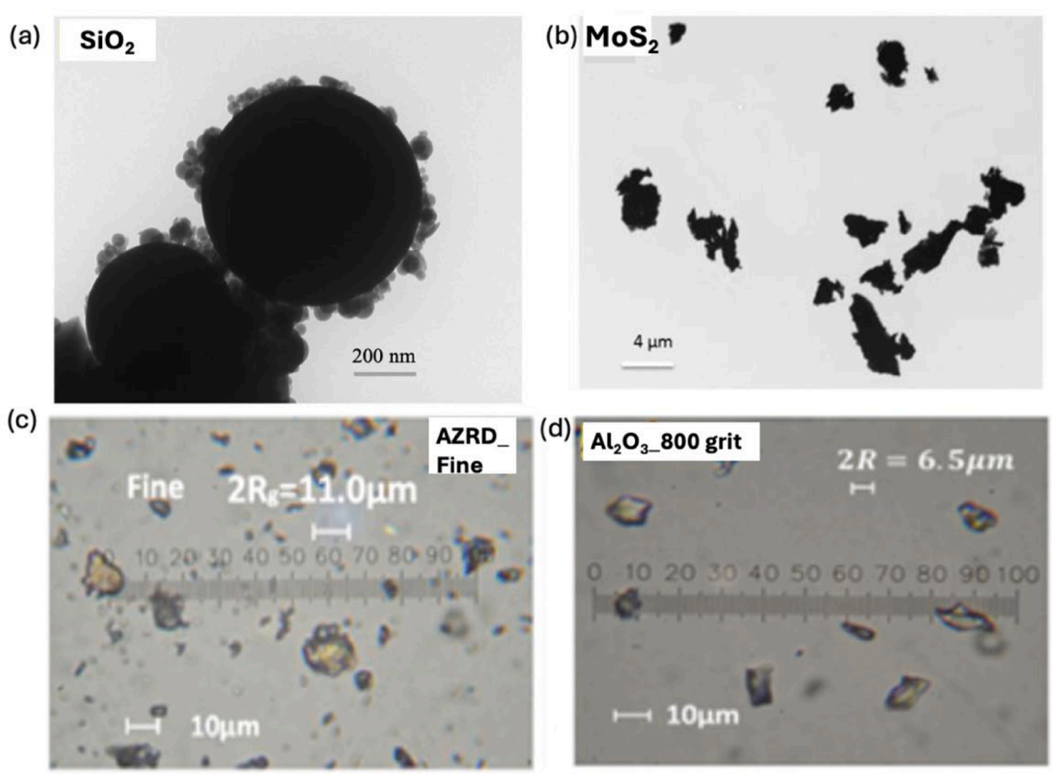

Fig. 1. Transmission electron microscope (TEM) images for a) spherical silica (SiO_2) and b) irregular molybdenum disulfide (MoS_2) particles, and optical microscope images for irregular c) Arizona Road Dust (Fine) and d) aluminum abrasive (Al_2O_3) grits [16].

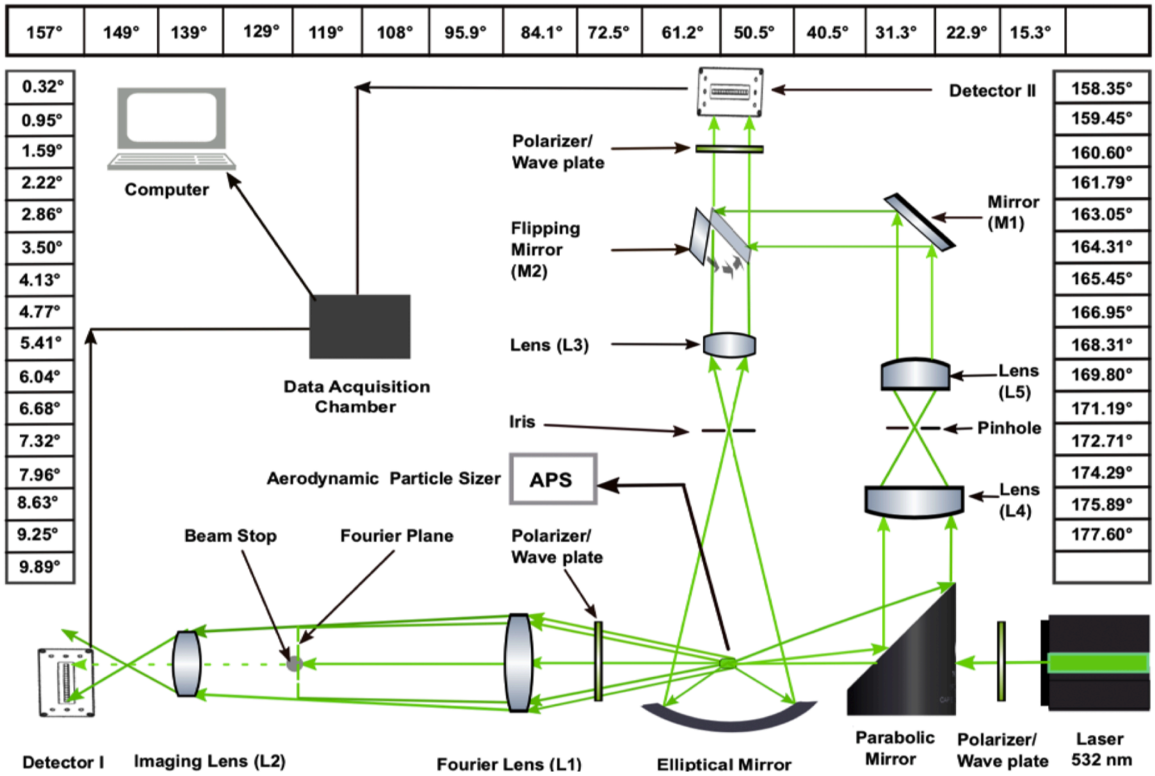

Fig. 2. Schematic diagram of the multi-angle light scattering apparatus.

$$\mathrm{LDR} = \frac{I_{VH}}{I_{VV}} \tag{1}$$

The LDR is also known as the linear polarization ratio, μ_L[21]. In Eq. (1), I_{VH} and I_{VV} are the intensity of scattered light measured with a linear horizontal and a linear vertical polarizer, respectively, for vertically polarized incident light. In terms of scattering matrix elements, the LDR of an ensemble of randomly oriented particles is given by [20] as

$$\mathrm{LDR} = \frac{1 - F_{22}/F_{11}}{1 + 2F_{12}/F_{11} + F_{22}/F_{11}} \tag{2}$$

with the LDR being a function of scattering matrix elements, F_{11}, F_{12}, and F_{22}. Here, Eq. (1) is used to measure the LDR experimentally as it provides a straightforward approach and Eq. (2) is utilized for theoretical calculations to interpret the experimentally obtained LDR measurements.

3. Results

Given the angular variation in the magnitude of LDR observed experimentally and theoretically, we propose that the best way to comprehensively explain the wide-angle LDR data is by dividing the angular range into three regimes: forward-, side-, and back-scattering. We have recently presented this segmentation for angular scattering intensity data [22]. In a similar approach, the LDR can be most efficiently studied by dividing the whole light scattering data into three distinct regimes, as follows:

1. The forward-scattering regime, $0 \leq \theta \leq 10^\circ$ in which LDR values are insignificantly small and fairly insensitive to the particle's microphysical properties: size, shape, and complex refractive index. It includes a region where $\theta < \frac{\lambda}{2R}$, with λ being the wavelength of the light used and R the radius of the particle. This regime can be classified as a diffraction-dominated regime.
2. The side-scattering regime, $10^\circ \leq \theta \leq (140^\circ - 160^\circ)$ is where LDR values typically show a pronounced increase as the scattering angle increases, peaking at around 140° to 160° before declining. This regime begins with a cross-over from diffraction-dominated to refraction-reflection-dominated scattering, resulting in an increased depolarization of the scattered light.
3. The back-scattering regime, $(140^\circ - 160^\circ) \leq \theta \leq 180^\circ$, is characterized by a gradual decrease in LDR values as function of scattering angle, followed by a chaotic looking, unexplained pattern, as the scattering angle approaches the exact backscattering angle, 180° This regime plays a key role in remote sensing.

Fig. 3 shows measured LDRs for two sizes of nearly spherical non-absorptive silica, SiO_2 (Fig. 3a), and highly absorptive irregular molybdenum disulfide, MoS_2 (Fig. 3b) particles. The CRIs for silica and molybdenum disulfide particles at $\lambda = 532$ nm are $m_{SiO_2} = n + ik = 1.46 + i0$ and $m_{MoS_2} = 5.24 + i1.16$, respectively [23]. The same data were plotted using both linear-linear (left) and log-linear (right) scales to better visualize the small values in the forward scattering regime, which are not visible in the linear-linear plot.

In the forward scattering regime, LDR values were found to be insignificant and negligible for both SiO_2 (Fig. 3a) and MoS_2 (Fig. 3b) particles, regardless of their different morphologies and CRIs. Diffraction dominance accounts for the negligible LDR values in this regime as diffraction does not alter the polarization irrespective of the particle's physical parameters.

In the side-scattering regime, the values of LDR increase as the scattering angle increases, reaching a maximum of ≈ 15 % for SiO_2 and ≈ 10 % for MoS_2 at approximately 140° to 160°. For a perfectly spherical particle, $F_{11} = F_{22}$ [20], which theoretically [Eq. (2)] implies that LDR values should be zero throughout the whole angular range. The finite LDR values observed for SiO_2 may be due to nano-size silica attaching to the micron size silica particles (Fig. 1a) thereby creating a distortion in sphericity as supported by the theoretical calculations shown in Fig. 3 (a). In Fig. 4(a), the LDR calculations for a Gaussian random sphere

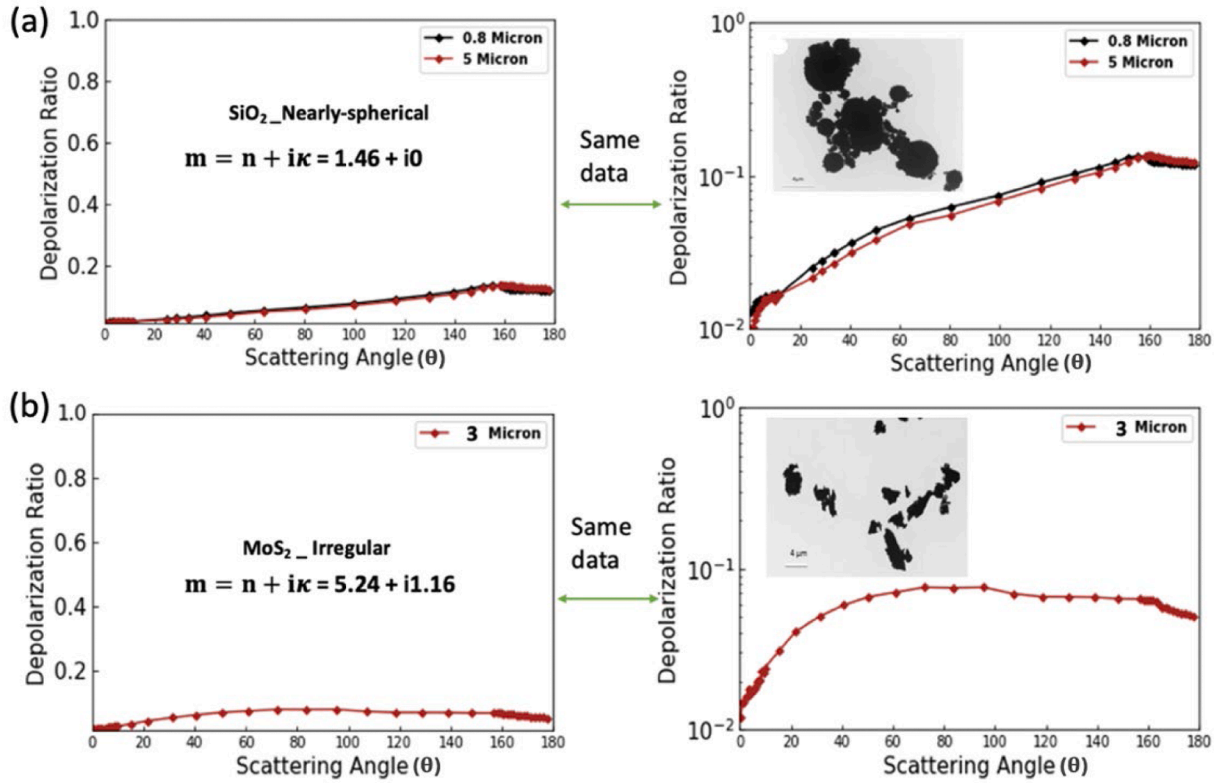

Fig. 3. Experimentally measured LDR for (a) two sizes of nearly spherical silica (SiO_2) (data are in close agreement) and (b) highly refractive irregular molybdenum disulfide (MoS_2) particles. The right column contains TEM images of these particles. The same data are plotted in linear (left column) and log-linear (right column) for visual clarity of the LDR pattern in the forward scattering regime. The experimental errors are not shown on the graph because they are too small to be represented.

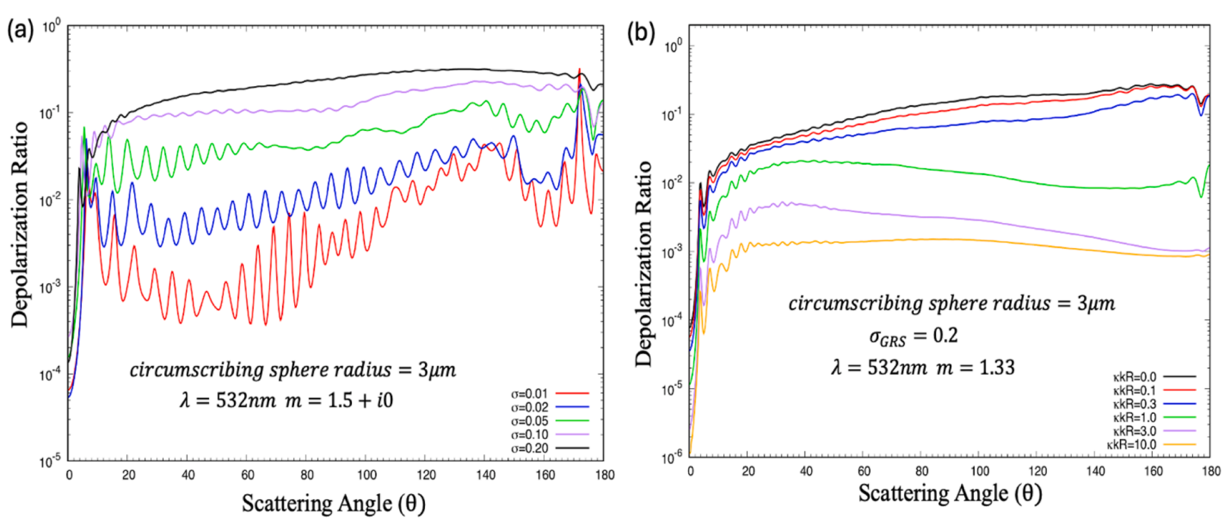

Fig. 4. Theoretically calculated LDRs for a Gaussian random sphere (GRS) with a circumscribing sphere radius of $r = 3$ μm, showing the change in (a) particle shape distortion, σ, from sphericity, and (b) the imaginary part of CRI, expressed as κ*kR*.

(GRS) with a circumscribing radius of 3 μm, equivalent to the mode size distribution measured by APS, show that LDR values increase with an increase in shape irregularity (σ). The shape irregularity corresponds to a relative deviation in the radial distance of the Gaussian sphere, which facilitates the straightforward treatment of non-spherical shapes with analytical results. The observed low LDR value for irregularly shaped MoS_2 particles (Fig. 3(b)) can be attributed to the large imaginary part of the MoS_2 CRI as illustrated by Fig. 4(b). Additionally, we calculated the LDR using high values of the real part and zero for the imaginary part of the complex refractive index. The results showed no decrease in LDR, confirming that the low LDR values observed for MoS_2 are primarily due to its high absorption (i.e., the imaginary part of the refractive index).

Fig. 4(b) demonstrates the effect of the imaginary part of the refractive index on the LDR values. To explore the LDR in absorbing particles (with finite $\kappa > 0$), we proposed calculating it in terms of κkR (the skin depth parameter) [24,25] which is the product of the imaginary parts of the refractive index (κ) and the size parameter ($kR = 2\pi R/\lambda$). The parameter κkR quantifies the relative penetration depth of light into the material, and in [25] it is shown that the effects of κ on the light scattering from absorptive particles can be universally described using this parameter. In Fig. 4(b), we present the LDR calculations for a Gaussian random sphere (GRS) with a circumscribing radius of 3 μm, considering various values of the imaginary part of the CRI, calculated as κkR. The results indicate that LDR values decrease as κkR increases and become negligible across the full angular scattering range when κkR exceeds unity. When $\kappa kR \geq 3$, incident light barely penetrates the particles, and refraction phenomena within the particles do not affect scattering, causing them to behave as opaque objects. These conclusions and explanations are consistent with our previous studies of [24–26]. Therefore, as the imaginary part, κ of the CRI increases, the LDR decreases, where κkR is the crucial factor in determining the LDR for absorbing particles.

In the back-scattering regime, experimental data consistently indicate a decline in LDR as a function of increasing scattering angle for all investigated particle types. However, the theoretical calculations (Fig. 4a) show a sharp increase in LDR near the exact backscattering angle of 180° as the irregularity, σ increases from nearly spherical (σ = 0.01) and for small κkR (≤1) (Fig. 4b). Further theoretical calculations shown in Fig. 7 for hexagonal and spheroidal particles with real refractive indices of $m = 1.33$ and 1.76, aspect ratios of 2, and varying sizes from $R = 0.12$ to 3.83 μm do not show such a sharp rise near the exact backscattering angle of 180° The spike in LDR was not seen in our experimental data, likely due to our inability to measure the last few degrees near the backscatter angle (i.e., 180°) with our light scattering setup. Near and exact backscattering LDR measurements using advanced optical setups can be found in [27]. However, based on both our theoretical calculations and experimental observations, the variation in LDR functionality with scattering angle in the backscattering regime suggests that two distinct regimes may exist in this domain. This regime appears to depend strongly on particle microphysical properties: shape, size/size distribution, and complex refractive index. The strong dependence of LDR on these properties, similar to the scattering phase function [28], leads to the conclusion that extrapolating LDR to the near and exact 180° backscattering angle may lead to inaccurate results. This study emphasizes the need for both experimental measurements and theoretical calculations of LDR across different particle microphysical properties to gain a clear and thorough understanding of LDR in the backscattering regime.

We conducted additional laboratory experiments with irregular Arizona Road Dust (AZRD) and aluminum oxide abrasive (Al_2O_3) particles of different sizes to examine the LDR across a wide range of particles, as illustrated in Figs. 5(a) and (b) for AZRD and Al_2O_3 particles, respectively. The same data were plotted using both linear-linear (left) and log-linear (right) scales to better visualize the small values in the forward scattering regime, which are not visible in the linear-linear plot. In the forward-scattering regime, where diffraction is the dominant factor, LDR values were very low (few percent) for both particle types. In the side-scattering regime, the LDR values increase with scattering angle, reaching a peak between 140° and 160° before declining. In the back-scattering regime, Al_2O_3 particles, which have a higher refractive index ($n = 1.76$), exhibit a noticeable drop in LDR as function of scattering angle compared to AZRD particles ($n = 1.54$). However, both particle types show a partial correlation between LDR and particle size, where larger particles tend to have higher LDR values and vice versa.

Additionally, we explored existing scattering data for different aerosol particles present in the Granada-Amsterdam (GA) light scattering database [10,14]. These data are shown in Fig. 6, and they exhibit a random and disordered LDR pattern, which can be attributed to the presence of various particles with different sizes and CRIs. The LDR patterns observed in the GA light scattering data (Fig. 6) are consistent with the results we measured experimentally (Figs. 3 and 5). The same data were plotted using both linear-linear (left) and log-linear (right)

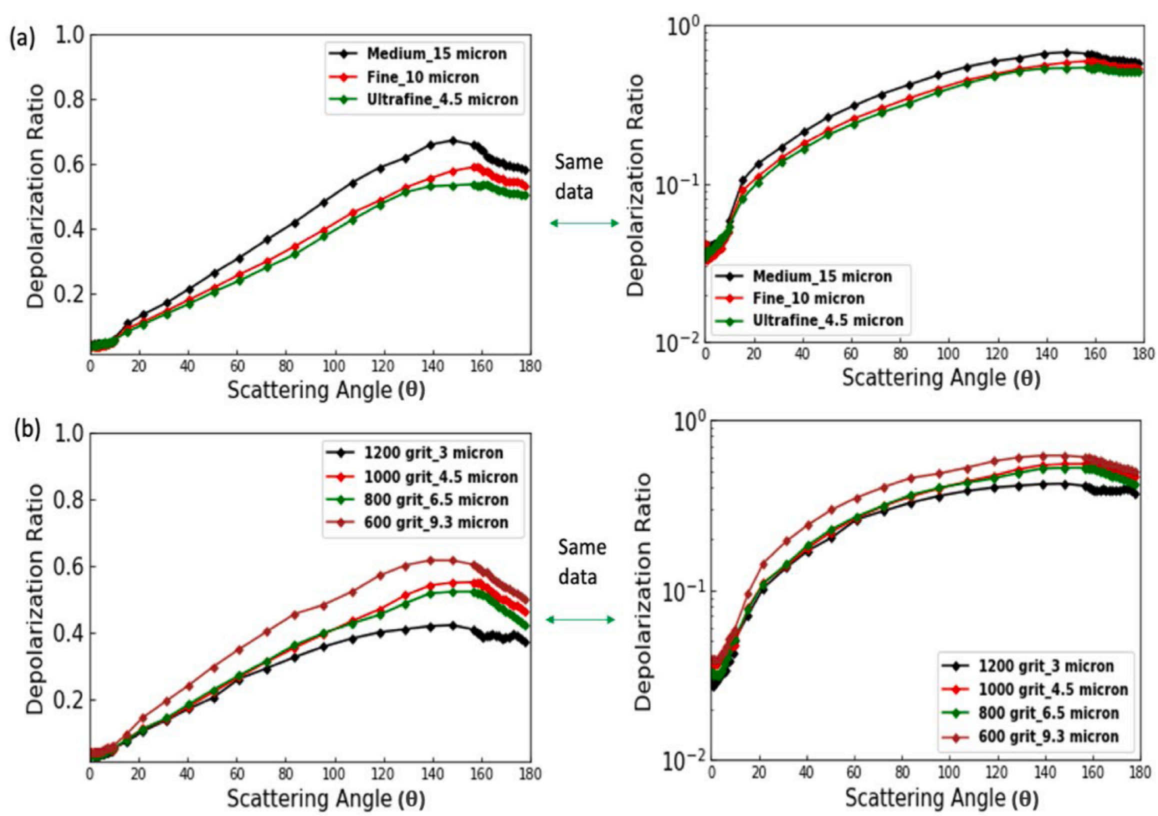

Fig. 5. Experimentally measured LDR for (a) three different sizes (Medium, Fine, and Ultrafine) of irregular Arizona Road Dust (AZRD) and (b) four different grit sizes (1200, 1000, 800, and 600 grit) of aluminum oxide abrasive (Al_2O_3) dust particles. The same data are plotted in linear (left column) and log-linear (right column) for visual clarity of the LDR pattern. The experimental errors are not shown on the graph because they are too small to be represented.

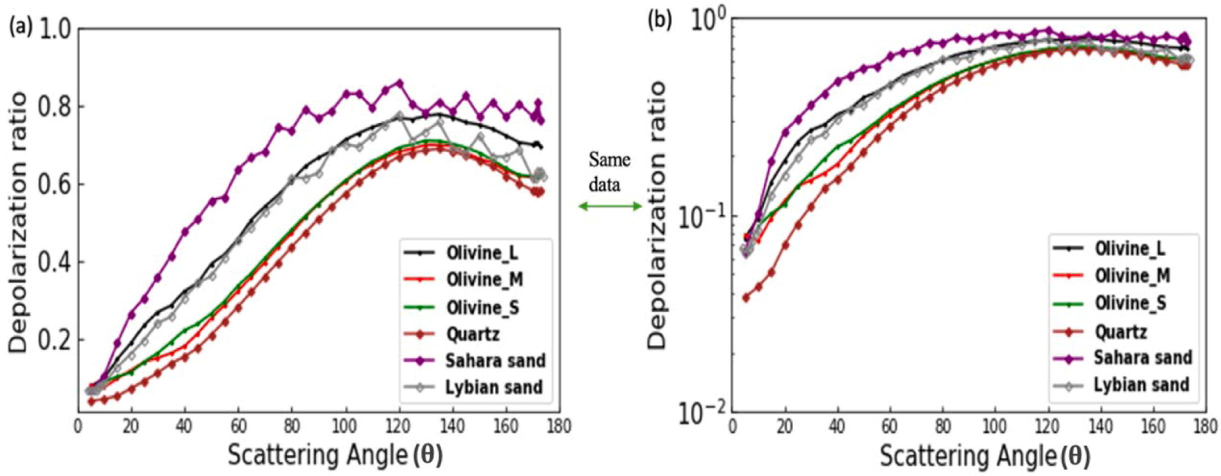

Fig. 6. Linear depolarization ratio for various aerosol particles presented in (a) linear, (b) log-linear scale as function of scattering angle, as reported by the Granada-Amsterdam (G/A) group (Munoz et al. 2000; Munoz et al., 2002; Munoz et al. 2004; Munoz et al. 2007; Volten et al. 2001; Volten et al. 2006) for Olivine L, Olivine M, Olivine S, Quartz measured at λ= 441.6 nm and for Saharan and Libyan sand measured at λ = 632.8 nm [10,14].

scales to better visualize the small values in the forward scattering regime, which are not visible in the linear-linear plot. Importantly, their measurements did not include the most important near-forward and near-exact back-scattering angles, as their setup was limited to measuring LDR across the scattering range from 3° to 177° Consequently, LDR values in the near-forward scattering regime for their dataset were limited to 3° and were not as small as for our datasets that included LDR values for angles down to 0.32°

For theoretically investigations of LDR and comparisons with experimental results, we used the numerically exact T-matrix method

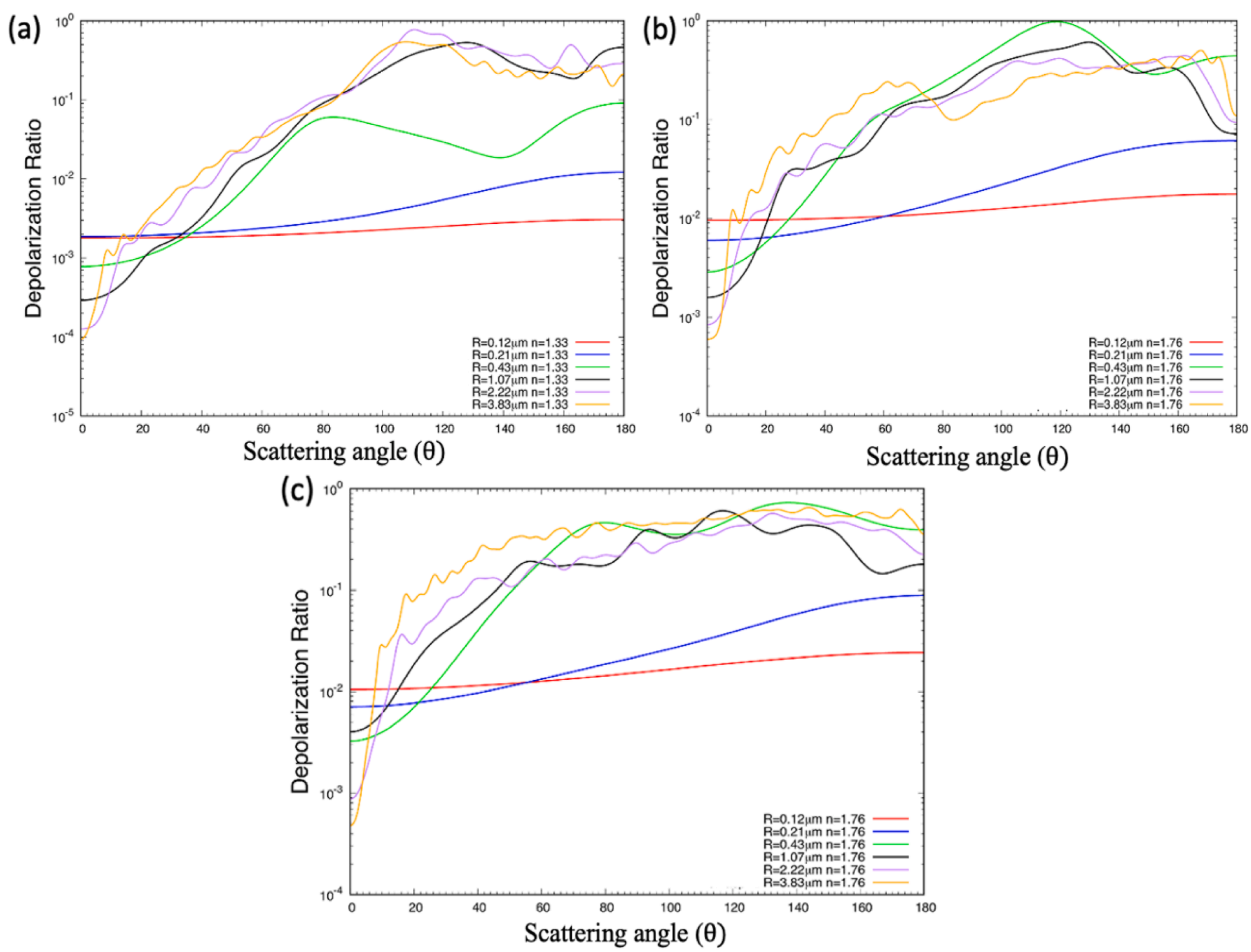

Fig. 7. Linear depolarization ratios for spheroidal particles with purely real refractive indices (a) $m = 1.33$, (b) $m = 1.76$, and for hexagonal particles with the purely real refractive index of $m = 1.76$, shown in (c). The aspect ratio is constant at asp = 2, with particle sizes varying from $R = 0.12$ to 3.83 μm.

[13]. We represented nearly spherical particles as Gaussian random sphere (GRS) and irregular dust particles as spheroids and hexagons. We further assumed particles are randomly oriented and form a statistically isotropic and mirror-symmetric ensemble. Figs. 7(a) and 7(b) show the LDR results for spheroids with a purely real refractive index of $n = 1.33$ and 1.76, respectively, whereas Fig. 7(c) shows the LDR results for hexagons with a purely real refractive index of $n = 1.76$. We kept the aspect ratio identical (asp = 2) for all these calculations but varied the sizes (R = 0.12 - 3.83 μm). We chose these two purely real refractive indices to cover the range of the real part of refractive indices for the particles investigated in this work. The LDR patterns obtained from theoretical calculations correspond well with the experimental data, Figs. 3 and 5, and G/A data (Fig. 6), above. However, the theoretical calculations show that the LDR varies non-linearly with the scattering angle across the entire angular scattering range, each varying independently with particles' microphysical properties: shape, size, and refractive index.

Fig. 8 shows the theoretical calculations to demonstrate how the individual scattering matrix elements F_{11}andF_{22} contribute to the LDRs for absorbing particles as function of the relative skin depth parameter, κkR. In Eq (2), the numerator of LDR goes as $1 - F_{22}/F_{11}$ so when $F_{11} \sim F_{22}$ the LDR trends toward 0. Conversely, when $F_{11} > F_{22}$, the ratio F_{22}/F_{11} will become small leading to the numerator of Eq (1) increasing. In Fig. 8, the $F_{11}$and F_{22} elements of the phase matrix of spheroids are plotted vs κkR at three different scattering angles, calculated using the T-Matrix code [29]. It can be seen in Fig. 8(a) that in the forward direction $F_{11} \sim F_{22}$ for all κkR, leading to a very small value for LDR as also shown in the previous figures of this work. In Fig. 8(b), $F_{11}$and F_{22} at a scattering angle of $\theta = 90°$ are plotted vs κkR and it can be seen that when $\kappa kR < 1$, $F_{11} > F_{22}$ leading to larger LDR values, but as κkR approaches unity, F_{11}andF_{22} approach each other, thereby causing the LDR to decrease with increasing κkR. Fig. 8(c) shows similar results as Fig. 8 (b) at a scattering angle of $\theta = 180°$. We carried out additional theoretical analyses for other particle geometries, including varying aspect ratios, and obtained consistent results demonstrating how F_{11} and F_{22} contribute to LDRs.

4. Conclusion

In this study, we explored the angular dependence of the linear depolarization ratio (LDR) for a variety of aerosol particles with diverse microphysical properties: size, shape, and complex refractive index. Our findings show that the LDR behaves distinctly across three scattering regimes: forward-, side-, and back-scattering. In the forward-scattering regime, diffraction is dominant, resulting in very low LDR values regardless of particle properties. In the side-scattering regime, the LDR increases with scattering angle, peaking between 140° and 160° and then decreasing. The back-scattering regime exhibits a decline in scattering beyond the mild peak near 140° to 160°, often ending with a non-descriptive, chaotic evolution as the scattering angle approaches 180°. However, this was not observed in the experiments, likely because the experimental setup could not measure the LDR at the final few degrees. The theoretical analysis using T-matrix calculations aligned well with our experimental data, showing that particle size, shape, and the complex refractive index significantly influence the LDR. For absorptive particles, an increase in the imaginary part of the refractive index led to a decrease in LDR, as quantified by the relative skin depth, κkR. These insights enhance our understanding of aerosol properties and provide

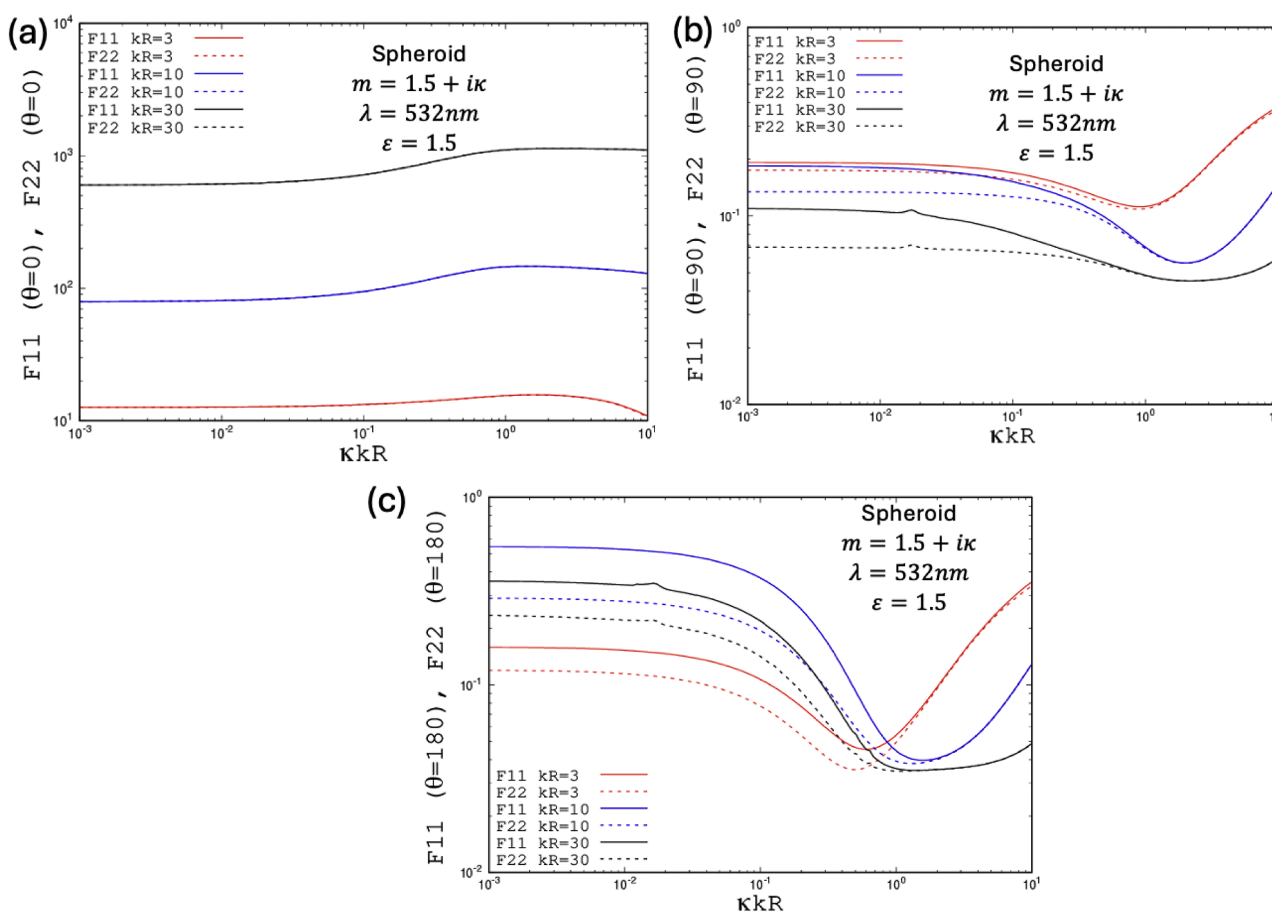

Fig. 8. F_{11} and F_{22} elements of the phase matrix vs. κkR for spheroids with an aspect ratio of 1.5, complex index of refraction given by m=1.5 + iκ, at a wavelength of λ=532 nm, and size parameters of kR=3, 10, and 30. These are plotted for three different scattering angles: (a) $\theta = 0°$, (b) θ=90°, and (c) θ=180°.

valuable guidance for future polarimetric studies in atmospheric and material characterization.

Funding

This work was funded in part by the Department of Energy Los Alamos National Laboratory through Kansas State University under Grant No A23–0465-S001, by the National Science Foundation under Grants No AGM-1649,783 and AGS-2516784 and No OIA-2148,788, by NASA PACE SAT Project No 23-PACE23–0053 through Columbia University, and by Nevada NASA Space Grant No 80NSSC20M0043.

CRediT authorship contribution statement

Prakash Gautam: Writing – original draft, Methodology, Investigation, Data curation, Conceptualization. **Justin B. Maughan:** Writing – review & editing, Methodology, Investigation. **Hans Moosmüller:** Writing – review & editing, Methodology, Investigation. **Kurt Ehlers:** Writing – review & editing, Methodology. **Christopher M. Sorensen:** Writing – review & editing, Supervision, Methodology, Conceptualization.

Declaration of competing interest

No potential conflict of interest was reported by the authors.

Data availability

The data used in this paper can be made available upon request to the corresponding author.

References

[1] Dubovik O, Li Z, Mishchenko MI, Tanré D, Karol Y, Bojkov B, et al. Polarimetric remote sensing of atmospheric aerosols: instruments, methodologies, results, and perspectives. J Quant Spectrosc Radiat Transf 2019;224:474–511. https://doi.org/10.1016/j.jqsrt.2018.11.024.

[2] Hamill P, Piedra P, Giordano M. Simulated polarization as a signature of aerosol type. Atmos Env 2020;224:117348. https://doi.org/10.1016/j.atmosenv.2020.117348.

[3] Kolgotin A, Müller D, Goloub P, Hu Q, Podvin T, Wang X. Aerosol typing from Linear estimations for the Analytical Separation (ATLAS) of complex aerosol mixtures and improved identification of microphysical parameters from multiwavelength lidar data, part 2: case studies. J Opt Soc Am JOSAA 2025;42:233–53. https://doi.org/10.1364/JOSAA.537287.

[4] Sakai T, Nagai T, Zaizen Y, Mano Y. Backscattering linear depolarization ratio measurements of mineral, sea-salt, and ammonium sulfate particles simulated in a laboratory chamber. Appl Opt AO 2010;49:4441–9. https://doi.org/10.1364/AO.49.004441.

[5] Wang Y, Chakrabarti A, Sorensen CM. A light-scattering study of the scattering matrix elements of Arizona Road Dust. J Quant Spectrosc Radiat Transf 2015;163:72–9. https://doi.org/10.1016/j.jqsrt.2015.05.002.

[6] Redding B, Pan Y-L, Wang C, Cao H. Polarization-resolved near-backscattering of airborne aggregates composed of different primary particles. Opt Lett 2014;39:4076–9. https://doi.org/10.1364/OL.39.004076.

[7] Muñoz O, Volten H, Hovenier JW, Min M, Shkuratov YG, Jalava JP, et al. Experimental and computational study of light scattering by irregular particles with extreme refractive indices: hematite and rutile. A&A 2006;446:525–35. https://doi.org/10.1051/0004-6361:20053727.

[8] Järvinen E, Kemppinen O, Nousiainen T, Kociok T, Möhler O, Leisner T, et al. Laboratory investigations of mineral dust near-backscattering depolarization ratios. J Quant Spectrosc Radiat Transf 2016;178:192–208. https://doi.org/10.1016/j.jqsrt.2016.02.003.

[9] Miffre A, Mehri T, Francis M, angle Rairoux PUV–VIS depolarization from Arizona Test Dust particles at exact backscattering. J Quant Spectrosc Radiat Transf 2016;169:79–90. https://doi.org/10.1016/j.jqsrt.2015.09.016.

[10] Muñoz O, Frattin E, Martikainen J, Guirado D, Passas-Varo M, Escobar-Cerezo J, et al. Update Granada–Amsterdam light scattering Database. J Quant Spectrosc Radiat Transf 2025;331:109252. https://doi.org/10.1016/j.jqsrt.2024.109252.

[11] Shkuratov Y, Bondarenko S, Ovcharenko A, Pieters C, Hiroi T, Volten H, et al. Comparative studies of the reflectance and degree of linear polarization of particulate surfaces and independently scattering particles. J Quant Spectrosc Radiat Transf 2006;100:340–58. https://doi.org/10.1016/j.jqsrt.2005.11.050.

[12] Schnaiter M, Büttner S, Möhler O, Skrotzki J, Vragel M, Wagner R. Influence of particle size and shape on the backscattering linear depolarisation ratio of small ice crystals - cloud chamber measurements in the context of contrail and cirrus microphysics. Atmos Chem Phys 2012;12:10465–84. https://doi.org/10.5194/acp-12-10465-2012.

[13] Mishchenko MI. Comprehensive thematic *T*-matrix reference database: a 2017–2019 update. J Quant Spectrosc Radiat Transf 2020;242:106692. https://doi.org/10.1016/j.jqsrt.2019.106692.

[14] Muñoz O, Moreno F, Guirado D, Dabrowska DD, Volten H, Hovenier JW. The Amsterdam–Granada light scattering Database. J Quant Spectrosc Radiat Transf 2012;113:565–74. https://doi.org/10.1016/j.jqsrt.2012.01.014.

[15] Heinson YW, Chakrabarti A, Sorensen CM. A light-scattering study of Al2O3 abrasives of various grit sizes. J Quant Spectrosc Radiat Transf 2016;180:84–91. https://doi.org/10.1016/j.jqsrt.2016.04.017.

[16] Gautam, P. 2022. Light scattering study of irregular particles with arbitrary size, shape, and complex refractive index Kansas State University. (PhD Thesis). https://krex.k-state.edu/handle/2097/42344.

[17] Gautam P, Sorensen CM. A wide range (0.32°–177.6°), multi-angle light scattering setup and concomitant analysis method. Rev Sci Instrum 2021;92:113105. https://doi.org/10.1063/5.0068318.

[18] Ferri F. Use of a charge coupled device camera for low-angle elastic light scattering. Rev Sci Instrum 1997;68:2265–74. https://doi.org/10.1063/1.1148135.

[19] Sorensen CM. Light Scattering. by 10.1088/978-0-7503-5157-7. Fractal aggregates: a review, 35. Aerosol Science and Technology; 2001. p. 648–87. https://doi.org/10.1080/02786820117868.

[20] Sorensen CM. Light scattering and absorption by particles: the Q-space approach. IOP Publishing; 2022. https://doi.org/10.1088/978-0-7503-5157-7.

[21] Mishchenko MI, Travis LD, Lacis AA. Multiple scattering of light by particles: radiative transfer and coherent backscattering. Cambridge University Press; 2006.

[22] Gautam P, Moosmüller H, Maughan JB, Sorensen CM. Light scattering from spherical and irregular particles over a wide angular range. Aerosol Sci Technol 2024;58:1053–62. https://doi.org/10.1080/02786826.2024.2338543.

[23] Gautam P, Sorensen CM. A light-scattering study of highly refractive, irregularly shaped MoS2 particles. J Quant Spectrosc Radiat Transf 2020;242:106757. https://doi.org/10.1016/j.jqsrt.2019.106757.

[24] Wang G, Chakrabarti A, Sorensen CM. Effect of the imaginary part of the refractive index on light scattering by spheres. J Opt Soc Am JOSAA 2015;32:1231–5. https://doi.org/10.1364/JOSAA.32.001231.

[25] Maughan JB, Sorensen CM. Universal parameter to describe the reduction of refraction effects in the scattering of absorbing spheres. J Opt Soc Am JOSAA 2020;37:1456–64. https://doi.org/10.1364/JOSAA.394401.

[26] Gautam P, Maughan JB, Ilavsky J, Sorensen CM. Light scattering study of highly absorptive, non-fractal, hematite aggregates. J Quant Spectrosc Radiat Transf 2020;246:106919.

[27] Aleau K, Ceolato R, Berg M, Huss G, Muñoz O, Videen G. Spectro-polarimetric backscattering of atmospheric particles. J Quant Spectrosc Radiat Transf 2024;327:109132. https://doi.org/10.1016/j.jqsrt.2024.109132.

[28] Gautam P, Moosmüller H, Maughan JB, Sorensen CM. Sensitivity of backscattering to spherical particle physical properties: size, refractive index, and shape deviations. J Quant Spectrosc Radiat Transf 2024;329:109204. https://doi.org/10.1016/j.jqsrt.2024.109204.

[29] Mackowski DW, Mishchenko MI. A multiple sphere T-matrix Fortran code for use on parallel computer clusters. J Quant Spectrosc Radiat Transf 2011;112:2182–92. https://doi.org/10.1016/j.jqsrt.2011.02.019.